Xueju Wang
Woodruff School of Mechanical Engineering,
Georgia Institute of Technology,
Atlanta, GA 30332

Zhipeng Pan
Woodruff School of Mechanical Engineering,
Georgia Institute of Technology,
Atlanta, GA 30332

Feifei Fan
Woodruff School of Mechanical Engineering,
Georgia Institute of Technology,
Atlanta, GA 30332

Jiangwei Wang
Department of Mechanical Engineering and
Materials Science,
University of Pittsburgh,
Pittsburgh, PA 15261

Yang Liu[1]
Center for Integrated Nanotechnologies,
Sandia National Laboratories,
Albuquerque, NM 87185

Scott X. Mao
Department of Mechanical Engineering and
Materials Science,
University of Pittsburgh,
Pittsburgh, PA 15261

Ting Zhu
Woodruff School of Mechanical Engineering,
Georgia Institute of Technology,
Atlanta, GA 30332

Shuman Xia[2]
Woodruff School of Mechanical Engineering,
Georgia Institute of Technology,
Atlanta, GA 30332
e-mail: shuman.xia@me.gatech.edu

Nanoscale Deformation Analysis With High-Resolution Transmission Electron Microscopy and Digital Image Correlation

We present an application of the digital image correlation (DIC) method to high-resolution transmission electron microscopy (HRTEM) images for nanoscale deformation analysis. The combination of DIC and HRTEM offers both the ultrahigh spatial resolution and high displacement detection sensitivity that are not possible with other microscope-based DIC techniques. We demonstrate the accuracy and utility of the HRTEM-DIC technique through displacement and strain analysis on amorphous silicon. Two types of error sources resulting from the transmission electron microscopy (TEM) image noise and electromagnetic-lens distortions are quantitatively investigated via rigid-body translation experiments. The local and global DIC approaches are applied for the analysis of diffusion- and reaction-induced deformation fields in electrochemically lithiated amorphous silicon. The DIC technique coupled with HRTEM provides a new avenue for the deformation analysis of materials at the nanometer length scales.
[DOI: 10.1115/1.4031332]

Keywords: digital image correlation, high-resolution transmission electron microscopy, deformation analysis, error assessment, lens distortion

1 Introduction

Full-field, noncontact deformation measurement is being increasingly used for the development and characterization of advanced materials and structures [1–7]. The technique of DIC has emerged as a particularly powerful tool for conducting such measurement due to its high accuracy and ease of use [8–11]. In a DIC analysis, the displacement distribution of a test specimen is obtained by correlation comparison between two high contrast digital speckle images taken from the deformed and undeformed states. The use of image correlation, as opposed to tracking the movement of individual pixels, allows full-field displacement data to be measured at the subpixel level. Combined with various optical imaging methods, DIC has been used for a wide spectrum of applications across multiple length scales, ranging from landslide monitoring using high-resolution satellite imagery [12] to microscale deformation analysis of biological tissues [13].

Driven by the recent advances in materials and biological research, there is a growing need for quantitative deformation analysis at the nanoscale. Due to the diffraction of visible light, the standard optical microscopy has a limited spatial resolution about half the light wavelength, thus invalidating the optical-based DIC method for nanoscale deformation measurement. To resolve this issue, attempts have been made to combine DIC with other high-resolution microscopy techniques. By performing DIC analysis of the surface topographies obtained from atomic force microscopy [14–23] and scanning tunneling microscopy (STM) [24–26], full-field deformation measurement techniques have been developed and applied for the mechanical property characterization at the micron and nanometer scales. More recently, DIC has been coupled with scanning electron microscopy (SEM) for quantitative deformation analysis [27–32]. It has been shown that compared to the optical DIC, the SEM-DIC approach is prone to drift and spatial distortions which need to be corrected with a nonparametric method to achieve high measurement accuracy. To further develop SEM-DIC, Kammers and Daly proposed new drift

[1]Present address: Department of Materials Science and Engineering, North Carolina State University, Raleigh, NC 27606.
[2]Corresponding author.

Contributed by the Applied Mechanics Division of ASME for publication in the JOURNAL OF APPLIED MECHANICS. Manuscript received June 20, 2015; final manuscript received August 15, 2015; published online September 10, 2015. Editor: Yonggang Huang.
The United States Government retains, and by accepting the article for publication, the publisher acknowledges that the United States Government retains, a nonexclusive, paid-up, irrevocable, worldwide license to publish or reproduce the published form of this work, or allow others to do so, for United States government purposes.

 Copyright © 2015 by ASME

Downloaded From: http://appliedmechanics.asmedigitalcollection.asme.org/ on 09/10/2015 Terms of Use: http://www.asme.org/about-asme/terms-of-use

distortion techniques accounting for stress relaxation [33] and used a novel speckle patterning method with self-assembled gold nanoparticles [34]. The SEM-DIC approach has shown potential in studying nanoscale thermal deformation [35], ductile fracture [36], and microstructure-property relationship [37,38].

Compared to the scanning probe and SEMs, the HRTEM offers a unique capability for characterizing internal material structures with subatomic spatial resolution [39,40]. Despite the widespread use of TEM for material characterizations, much of the TEM work till date has been focused on direct imaging and crystallographic analysis. Notably, increasing efforts are devoted to applying TEM for quantitative deformation measurement. A full-field method based on the Fourier analysis of HRTEM images was developed by Hÿtch et al. [41,42] to measure displacement and strain fields of a crystal lattice over a 25×25 nm area. The same group of authors recently reported a new method, namely, the dark-field electron holographic moiré technique [43], which offers larger fields of view without sacrificing measurement precision. Using electron diffraction under TEM, various studies have also been undertaken for the point-by-point measurement of localized strains in semiconductor materials with the strain measurement sensitivity of 10^{-4} and spatial resolution of < 10 nm [44–48].

In this paper, we present a study of full-field deformation analysis by combining DIC and HRTEM. Owing to the subangstrom spatial resolution of HRTEM and the subpixel displacement measurement sensitivity associated with DIC, the HRTEM-DIC analysis provides unprecedented nanoscale characterization capabilities that are not possible with optical and SEM-based DIC. To the best of our knowledge, this work represents the first systematic attempt to apply DIC to the quantitative full-field analysis of TEM images. In an effort to quantify the levels of DIC errors induced by the TEM image noise and electromagnetic-lens distortions, we performed experiments of rigid-body motion using amorphous silicon (*a*-Si) as a model material. The random atomic structure inherent in *a*-Si allows image correlation to be performed without the need of dedicated speckle patterning. For other materials lacking such intrinsic random feature, speckle patterning techniques such as ion implantation with a foreign species [49] may be employed. To further demonstrate its utility, we applied the HRTEM-DIC analysis to investigate a recently discovered mechanism of two-phase lithiation in *a*-Si [50]. The remainder of this paper is organized as follows. In Sec. 2, we present the general theory behind two different DIC schemes—local and global DIC—which are used for TEM image correlation in this study. Section 3 provides the details of *a*-Si sample preparation and TEM experiments. The results of quantitative error assessment and deformation analysis in lithiated *a*-Si are presented and discussed in Sec. 4. Finally, the conclusions are drawn in Sec. 5.

2 Theory

In a two-dimensional DIC analysis, a full-field displacement distribution is obtained by correlating two digital gray-scale speckle images of a test specimen obtained before and after deformation [8,51,52]. The correlation is based on the assumption that the gray level is conserved at all pixel locations during deformation. Let f and g be the images in the reference and deformed configurations, respectively. The conservation law at a pixel location in the reference image, $\mathbf{X}$, can be given as

$$f(\mathbf{X}) = g(\mathbf{X} + \mathbf{U}(\mathbf{X})) \tag{1}$$

where $\mathbf{U}(\mathbf{X})$ is the displacement vector at $\mathbf{X}$.

In the original DIC approach, the displacement field is obtained by partitioning the region of interest (ROI) in the reference image into an array of uniformly spaced subsets (usually square shaped) and tracking the movement of these subsets. The local deformation kinematics within a subset, S, is usually approximated in a linearized form as

$$\mathbf{U}(\mathbf{X}) \approx \mathbf{U}(\mathbf{X}_0) + \nabla\mathbf{U}(\mathbf{X}_0) \cdot (\mathbf{X} - \mathbf{X}_0) \tag{2}$$

in which $\mathbf{X}_0$ is the center of the subset, and $\mathbf{U}(\mathbf{X}_0)$ and $\nabla\mathbf{U}(\mathbf{X}_0)$ are the displacement and its gradient at $\mathbf{X}_0$, respectively. In Eq. (2), it is assumed that the deformation within the subset is close to be homogeneous so that the higher-order gradient terms can be neglected. Then, $\mathbf{U}(\mathbf{X}_0)$ is obtained by maximizing a cross-correlation function with respect to $\mathbf{U}(\mathbf{X}_0)$ and $\nabla\mathbf{U}(\mathbf{X}_0)$ according to

$$C = \frac{\int_S f(\mathbf{X}) \cdot g(\mathbf{X} + \mathbf{U}(\mathbf{X})) d\mathbf{X}}{\left\{ \int_S f(\mathbf{X})^2 d\mathbf{X} \cdot \int_S g(\mathbf{X} + \mathbf{U}(\mathbf{X}))^2 d\mathbf{X} \right\}^{1/2}} \tag{3}$$

It is worth noting that some DIC algorithms employ higher-order gradient terms in Eq. (2) to improve the accuracy of correlation [53,54]. In Eq. (3), the coordinates of the points in the deformed subset can be noninteger multiples of pixel. Therefore, the gray levels of these points need to be calculated through a pixel interpolation scheme. The most commonly used interpolation schemes in the literature include bilinear interpolation, bicubic interpolation, and bicubic spline interpolation [25,52,55]. By performing the above maximization independently for all subsets, a full-field displacement map of the test specimen can be constructed. Due to the use of the cross-correlation function in Eq. (3), the displacement measurement is highly immune to image noises and can achieve subpixel accuracy.

Recently, a new DIC method, which is conceptually different from the above subset-based local method, was developed based on a global description of the deformation kinematics over the whole ROI [56,57]. The global DIC method relies on minimizing the following sum-squared difference function:

$$\Phi = \int_{\mathrm{ROI}} [f(\mathbf{X}) - g(\mathbf{X} + \mathbf{U}(\mathbf{X}))]^2 d\mathbf{X} \tag{4}$$

To formulate the minimization problem, the true displacement field is approximated by a trial displacement field with a finite number of degrees of freedom. A straightforward choice among many possible ones is to follow the finite-element framework and express the trial displacement field as

$$\mathbf{U}_{\mathrm{Trial}}(\mathbf{X}) = \sum_{i=1}^{n} N_i(\mathbf{X})\mathbf{U}_i \tag{5}$$

in which $N_i(\mathbf{X})$ are the polynomial shape functions associated with a finite-element mesh with n nodes, and $\mathbf{U}_i$ are the nodal displacements. This formulation turns the DIC problem into a nonlinear, multivariable minimization of Φ with respect to $\mathbf{U}_i$, which can be well solved numerically using a Newton or gradient-descent iterative procedure. The final values of the nodal displacements are interpolated according to Eq. (5) to provide a full-field measure of the deformation within the ROI.

An alternative choice for the trial displacement field is to assume an analytical form as follows, based on a priori knowledge of the deformation field under analysis:

$$\mathbf{U}_{\mathrm{Trial}}(\mathbf{X}) = \mathbf{U}_{\mathrm{Ana}}(\mathbf{X}, \alpha_1, ..., \alpha_m) \tag{6}$$

where $\alpha_i (i = 1, ..., m)$ are the unknown parameters that are used to describe the displacement field. These parameters can be determined by the same minimization process as above, with α_i in place of $\mathbf{U}_i$ as the minimization variables. This scheme was recently employed by Réthoré et al. [58,59] to determine the stress intensity factors (SIFs) at a crack tip inside an elastic body. In their study, an analytical trial displacement field is assumed around a crack tip using the Williams asymptotic expansion [60], with α_i being the modes I and II SIFs and other higher-order coefficients in the Williams expansion.

In several recent case studies [61,62], global DIC and subset-based local DIC are thoroughly evaluated and compared to each

Downloaded From: http://appliedmechanics.asmedigitalcollection.asme.org/ on 09/10/2015 Terms of Use: http://www.asme.org/about-asme/terms-of-use

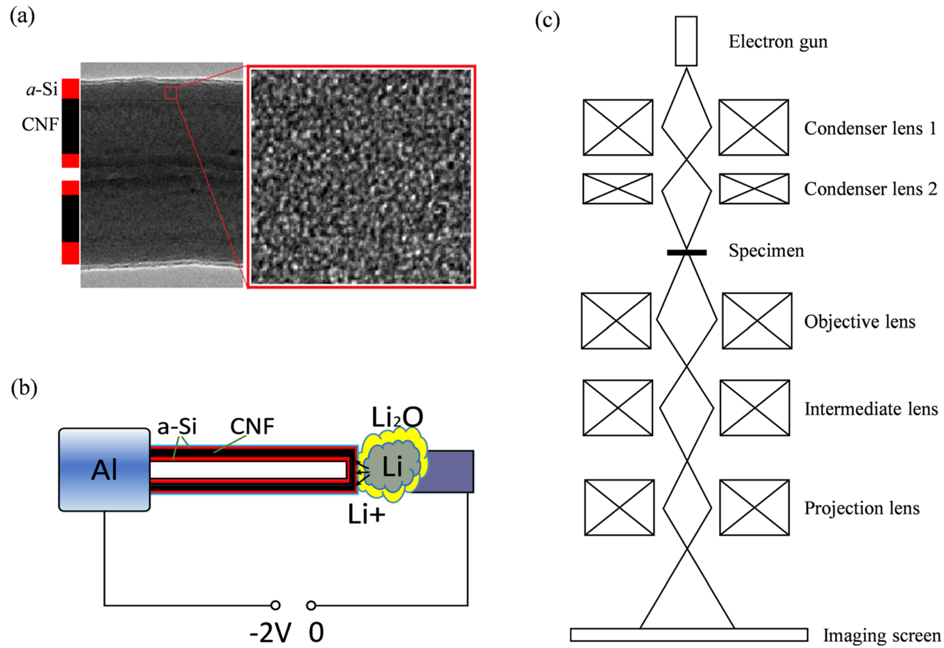

Fig. 1 (*a*) A TEM image showing the random atomic structure in amorphous silicon (*a*-Si), which serves as a high-quality speckle pattern for DIC analysis. (*b*) Schematic illustration of an in situ electrochemical lithiation experiment inside a TEM. (*c*) Schematic ray diagram of a TEM.

other. It is shown that, when applied to analyze weakly to moderately inhomogeneous deformation, the subset-based local DIC in general outperforms global DIC in terms of accuracy and computational efficiency. Nevertheless, the local DIC is less suitable for analyzing highly heterogeneous deformation, since the local heterogeneous deformation within a subset cannot be well captured with the finite-order kinematics as assumed by local DIC. Such cases are better handled using global DIC which is able to capture more complex deformation modes. In the present work, we combine both types of DIC in the analysis of the deformation associated with two-phase lithiation in *a*-Si. We employ local DIC to measure smooth strain maps induced by lithium (Li) diffusion in the amorphous lithiated silicon (*a*-Li_xSi) region. Across the sharp phase boundary between the *a*-Si and *a*-Li_xSi regions, there is a large deformation gradient due to the reaction of *a*-Si with lithium. Accordingly, we turn to a global DIC scheme assuming an analytical trial displacement function, which will be introduced later, to obtain the reaction-induced strain at the phase boundary.

3 Experimental

3.1 Sample Preparation. The *a*-Si samples used in this study were prepared by coating 20-nm thick *a*-Si layers onto both the

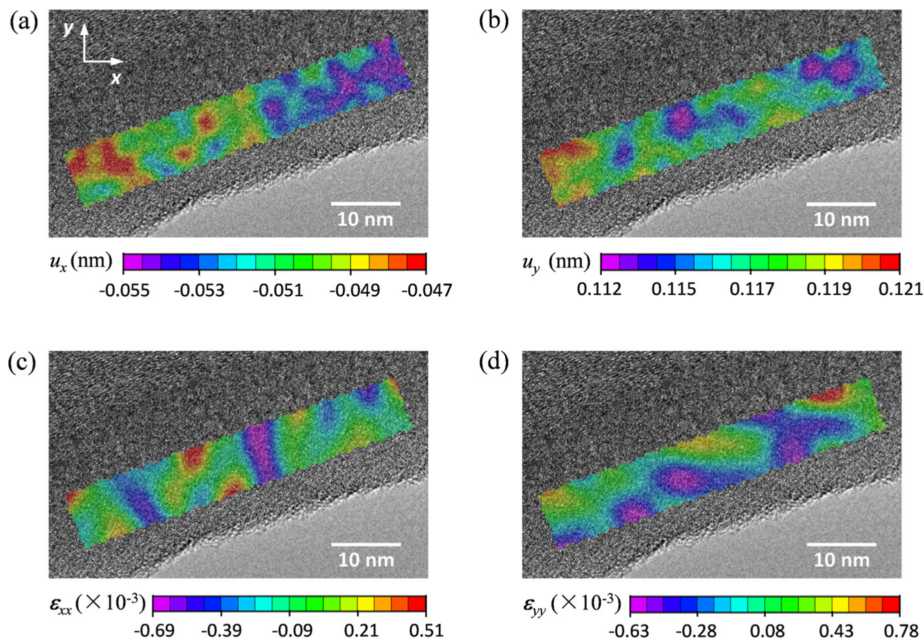

Fig. 2 Assessment of the DIC errors due to the TEM image noise. Maps of ((*a*) and (*b*)) displacements and ((*c*) and (*d*)) DIC strain errors resulting from the TEM image noise.

Downloaded From: http://appliedmechanics.asmedigitalcollection.asme.org/ on 09/10/2015 Terms of Use: http://www.asme.org/about-asme/terms-of-use

Table 1 Statistical characteristics of the displacement and strain maps shown in Figs. 2–4

	u_x (nm)		u_y (nm)		ε_{xx} ($\times10^{-3}$)		ε_{yy} ($\times10^{-3}$)	
	Mean	SD	Mean	SD	Mean	SD	Mean	SD
Figure 2	−0.051	0.002	0.116	0.002	−0.102	0.248	−0.046	0.311
Figure 3	2.633	0.007	−1.785	0.006	−0.514	0.742	0.076	0.761
Figure 4	3.515	0.007	−0.958	0.005	−0.400	0.676	0.037	0.642

inner and outer surfaces of hollow carbon nanofibers (CNFs) with the chemical vapor deposition method. The amorphous atomic structure of *a*-Si, as shown in Fig. 1(*a*), served as a random speckle pattern that was essential to image correlation. To prepare specimens for electrochemical lithiation experiments, a nanosized battery was constructed in the half-cell configuration, which consisted of a working electrode, a counter electrode, and a solid electrolyte. As schematically shown in Fig. 1(*b*), an *a*-Si/CNF composite nanowire was glued to an aluminum rod with conductive silver epoxy and used as the working electrode. On the surface of the *a*-Si layer, a 3-nm thick amorphous carbon (*a*-C) layer was coated to promote lithium ion and electron transport along the longitudinal direction. A lithium metal attached to a tungsten (W) probe was used as the counter electrode. A thin layer of LiO_2 (about 700 nm) on the lithium surface acted as the solid electrolyte.

3.2 TEM Experiments. A high-resolution TEM (FEI Tecnai F30) was used for in situ imaging of the *a*-Si specimens that were subjected to rigid-body translation or electrochemical lithiation. To set the stage for the results that will be presented below, it is necessary to briefly review the working principle of a TEM. Figure 1(*c*) shows the schematic outline of a typical TEM, which largely resembles that of an optical transmission microscope. The electron beam from an electron emitter is illuminated onto a thin sample with a set of electromagnetic condenser lenses. The electron beam interacts with the sample and partially transmits through it. The transmitted beam, after passing a series of objective, intermediate and projection lenses, is projected onto a fluorescent screen to create a magnified image that represents the internal structure of the sample. Similar to optical light microscopy, the TEM can operate in a variety of imaging modes including bright-field, dark-field, and phase-contrast imaging. In this work, we used the phase-contrast imaging mode due to its ultrahigh spatial resolution (~0.1 nm).

We performed two sets of experiments for TEM-DIC analysis. The first set of experiments was designed to assess the DIC errors related to different sources. In these experiments, an *a*-Si/CNF composite nanowire was supported on a copper grid which was mounted in a single-tilt TEM holder. An *a*-Si region in the nanowire was selected and imaged, while the nanowire was held still or subjected to rigid-body movement using the TEM sample stage. In the second set of experiments, we applied the TEM-DIC technique to analyze the lithiation-induced deformation in *a*-Si. A nanobattery as described in Sec. 3.1 was assembled and mounted into a Nanofactory TEM-STM holder in a helium-filled glovebox, where O_2 and H_2O concentrations were controlled below 0.1 ppm to avoid oxidation of the lithium. The holder was then transferred in a helium-filled plastic bag and inserted into the TEM column. During this process, the lithium metal was exposed to the air for about 5 s to form a Li_2O solid electrolyte layer. Inside the TEM, the Li_2O/Li terminal was driven by a piezo-positioner to engage the *a*-Si/CNF terminal. After the contact between the two terminals was established, the relative position of the tungsten probe with respect to the aluminum rod was held the same. A bias voltage of −2 V was applied to the *a*-Si/CNF electrode to drive the electrochemical lithiation process. During the lithiation, a sequence of high-resolution TEM images of the *a*-Si/CNF electrode was taken at an interval of 3–5 s. All TEM images taken in this study had the same pixel resolution of 0.077 nm. The *z*-height of the sample and the focusing condition for TEM imaging were kept unchanged during each experiment, in order to prevent their influences on the contrast of TEM images.

4 Results and Discussion

4.1 Error Assessment. Measurement errors can arise from several different sources in a TEM-DIC analysis. Digital images

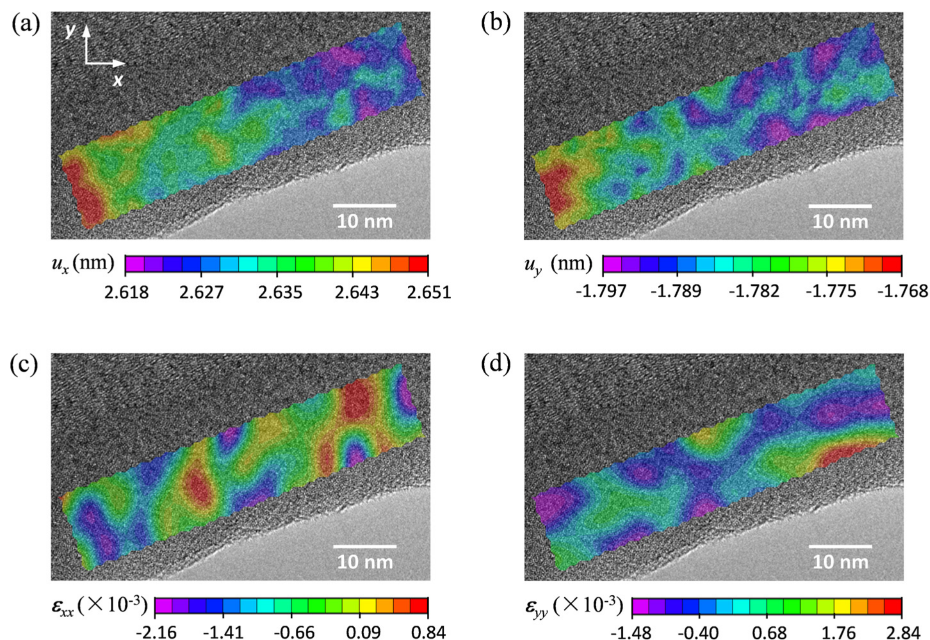

Fig. 3 Assessment of the DIC errors due to the electromagnetic-lens distortion. Maps of ((*a*) and (*b*)) displacements and ((*c*) and (*d*)) DIC strain errors resulting from a rigid-body translation of the *a*-Si sample.

Downloaded From: http://appliedmechanics.asmedigitalcollection.asme.org/ on 09/10/2015 Terms of Use: http://www.asme.org/about-asme/terms-of-use

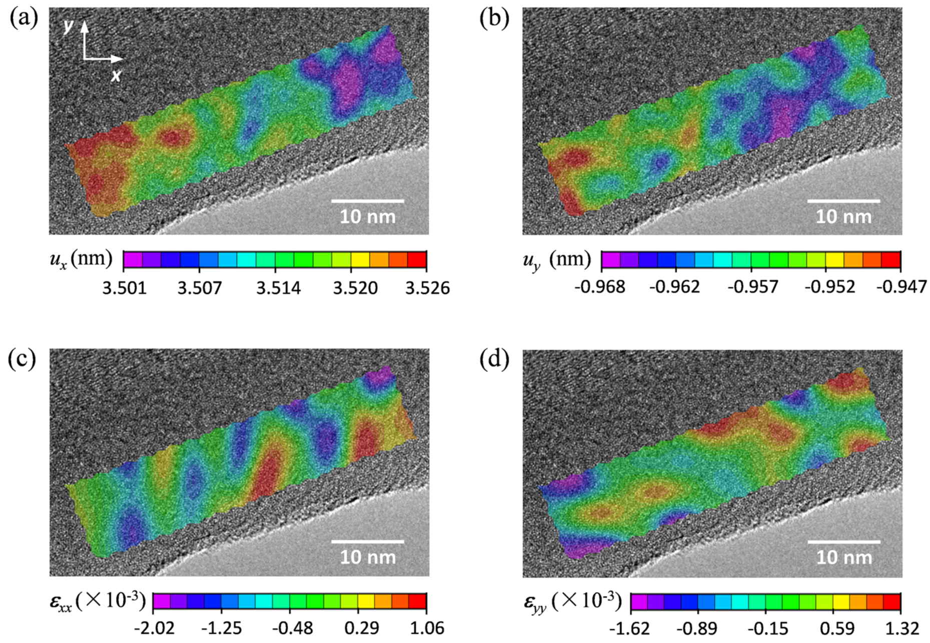

Fig. 4 Assessment of the DIC errors due to the image shift operation. Maps of ((*a*) and (*b*)) displacements and ((*c*) and (*d*)) DIC strain errors resulting from a rigid-body shift of the imaging window.

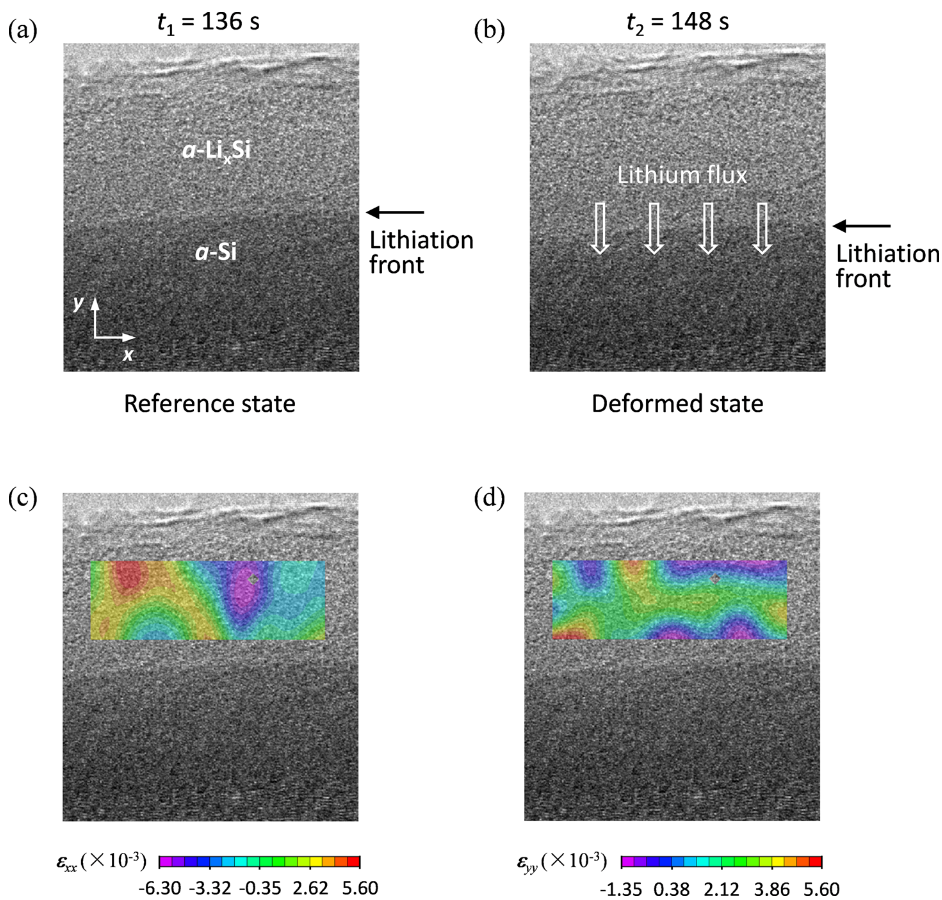

Fig. 5 Local DIC analysis of the lithium-diffusion-induced strain in a lithiated Si region. ((*a*) and (*b*)) Reference and deformed TEM images used for the DIC analysis. ((*c*) and (*d*)) Obtained ε_{xx} and ε_{yy} strain contour plots superimposed on the reference TEM image as shown in (*a*).

Downloaded From: http://appliedmechanics.asmedigitalcollection.asme.org/ on 09/10/2015 Terms of Use: http://www.asme.org/about-asme/terms-of-use

obtained from TEM experiments usually contain undesired pixel noise originating from the shot noise of the electron source, the electronic noise of the detector [63], as well as the environmental noise [64]. Such pixel noise results in a degradation of the pixel intensity conservation law (Eq. (1)) and therefore can cause appreciable errors in the image correlation. Another common type of error is due to the geometric distortion of the TEM imaging system. Unlike the distortion of optical lenses, which is relatively easy to correct using parametric distortion models, the electromagnetic-lens distortion of a TEM poses a greater challenge to model and compensate. In this study, we employed several testing procedures to quantitatively assess the levels of noise and distortion-induced errors. However, the correction of such errors is beyond the scope of the present work and will be left for future consideration.

We first quantified the noise-induced errors by correlating two TEM images of the same a-Si region in a nanowire. The two images were acquired 1 s apart while keeping the sample stationary. The DIC analysis was conducted using subset-based commercial software (VIC-2D, Correlated Solution, Inc., West Columbia, SC). A subset size of 59×59 pixels and a step size of 10 pixels were chosen for the analysis. The subset size was made much larger than the speckle size to reduce the effects of image noise, since TEM images usually have a higher noise level than typically seen in optical images. Also, to avoid the edge effects, the boundary points at a distance of less than half the subset size from the ROI boundary are excluded for all the local DIC analysis reported in this paper. The obtained displacement and strain maps are presented in Fig. 2. Although no external displacement was applied to the sample, the horizontal (u_x) and vertical (u_y) displacement components in Figs. 2(*a*) and 2(*b*) show small but non-negligible values with means of -0.05 and 0.12 nm, respectively. This displacement was caused by the creeping movement of the sample stage and/or the thermal drift of the TEM components. As a result of the random Gaussian noise inherent in the TEM images, the two displacement maps show fluctuations of 0.002 nm (0.026 pixel) as measured by their respective standard deviations (SDs). The fluctuations in displacement lead to nonzero strain distributions (ε_{xx} and ε_{yy}) with SDs of 0.02–0.03% as shown in Figs. 2(*c*) and 2(*d*). The statistical characteristics of the noise-induced displacement and strain maps are summarized in Table 1, together with those of other maps that will be discussed below.

The errors induced by the electromagnetic-lens distortion were assessed through rigid-body sample translation and image shift. We first subjected an a-Si sample to a rigid-body translation and measured the associated displacement. The sample translation was achieved by moving the motorized sample stage for a nominal horizontal displacement of about 3 nm. Figures 3(*a*) and 3(*b*) show the measured distributions of u_x and u_y. The u_y component is found to have a small deviation from its zero nominal value due to the crosstalk of the sample stage. In similar rigid-body translation experiments conducted at much larger length scales, the DIC error is usually calculated as the bias of the measured displacement from the true one. However, in this TEM experiment, the true displacement imposed on the sample is in the nanometer range and is therefore difficult to determine precisely. To resolve this issue, we consider a combination of several statistical parameters, including the absolute mean strain components ($|\varepsilon_{xx}^{\mathrm{m}}|$ and $|\varepsilon_{yy}^{\mathrm{m}}|$) and the SDs of displacement and strain (σ_{u_x}, σ_{u_y}, $\sigma_{\varepsilon_{xx}}$, and $\sigma_{\varepsilon_{yy}}$), as the measure of error (MOE). All of these parameters should be zero in the error-free case and increase with an increasing level of DIC errors. Table 1 shows the MOE parameters calculated from Fig. 3. These parameters show a two- to three-fold increase compared to those solely resulting from the image noise, thereby quantitatively indicating the presence of electromagnetic-lens distortion. Note that the DIC strain error maps in Figs. 3(*a*)–3(*d*) are highly irregular in appearance, suggesting that a parametric model may not be practical for lens-distortion correction.

TEM imaging at high magnifications is susceptible to sample drift which can cause the area of interest (AOI) in a sample to move out of the field of view. Modern TEMs offer an "image shift" function to compensate such drift by steering the electron beam to a targeted AOI with a set of electromagnetic deflection coils. The image shift procedure may lead to additional electromagnetic-lens distortion and therefore introduce measurement error for image correlation. We assessed this type of error by holding an a-Si sample still and applying an image shift of 3.5 nm in the horizontal direction. Figure 4 shows the maps of apparent displacement and strain associated with this shift. The variations in these maps are much greater than those in Fig. 2 resulting from the image noise only. Comparing the MOE parameters presented in Table 1, the strain errors induced by the image shift and rigid-body sample translation are found to be at similar levels of $\sim$0.1%. In order to obtain physically meaningful deformation fields using local DIC, one has to make sure that the strain under analysis is sufficiently larger than this error level.

4.2 Nanoscale Deformation Measurement in Lithiated a-Si.

To demonstrate its utility, we applied TEM-DIC to quantitatively analyze a two-phase lithiation process in a-Si. In the development of next-generation rechargeable lithium-ion batteries (LIBs), a current challenge is to understand the mechanical characteristics of high-capacity electrode materials. Using in situ TEM, we recently investigated the lithiation-induced deformation in a-Si as a high-capacity LIB anode material. We revealed a striking two-phase lithiation process in a-Si [50], which is contrary to the widely held view that the lithiation in a-Si is a single-phase process with gradual and smooth lithium profiles.

Figures 5(*a*) and 5(*b*) show two high-resolution TEM images taken at different time instants during an electrochemical

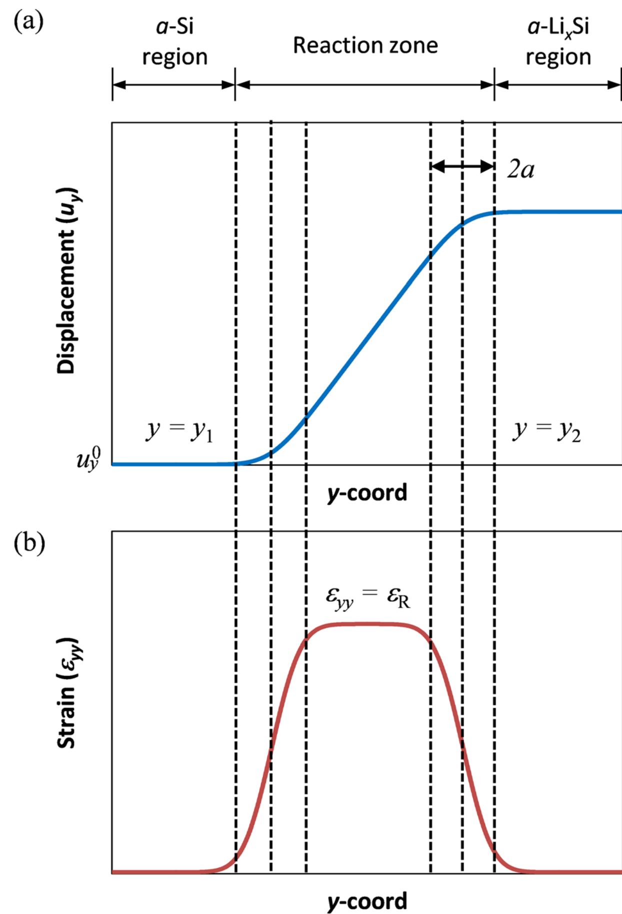

Fig. 6 Plots of the trial (*a*) displacement and (*b*) strain functions used for the global DIC analysis of the reaction-induced strain at an *a*-Si/*a*-Li$_x$Si phase boundary

Downloaded From: http://appliedmechanics.asmedigitalcollection.asme.org/ on 09/10/2015 Terms of Use: http://www.asme.org/about-asme/terms-of-use

lithiation experiment. The lithium flux was supplied from the top surface. The lithiation is seen to proceed by the movement of a sharp phase boundary between the a-Si reactant and an amorphous a-Li_xSi product. The growth kinetics of a-Li_xSi is controlled by two concurrent processes: (1) the *reaction* of Li with Si to form an initial product of Li_xSi at the phase boundary and (2) the *diffusion* of the Li ions in the product phase region. We employed the local DIC method to analyze the diffusion-induced strain in the a-Li_xSi region behind the phase boundary. The image at $t_1 = 136$ s (Fig. 5(*a*)) was chosen as the reference configuration and the image at $t_2 = 148$ s (Fig. 5(*b*)) as the deformed configuration. Figures 5(*c*) and 5(*d*) present the distributions of the two normal strain components obtained from DIC analysis. The two strain maps show fluctuations with statistical means and SDs of $\varepsilon_{xx} = (-0.06 \pm 2.93) \times 10^{-3}$ and $\varepsilon_{yy} = (1.82 \pm 1.49) \times 10^{-3}$. The levels of both strain components are comparable to the strain errors induced by the image noise and lens distortion, indicating the two strain maps should be interpreted as DIC errors rather than true deformation. This result also suggests that the diffusion-induced strain is negligibly small (relative to the measurement capability), and therefore, nearly all of the lithiation-induced deformation occurs at the sharp reaction front. It is noteworthy to mention that, to enable DIC analysis, the shape of the speckle pattern should not change significantly during the deformation. In our work, the random atomic structure of Si in the a-Li_xSi region is not expected to undergo substantial change, due to the very small mobility of Si compared to that of Li. On the other hand, the atomic-scale distribution of Li ions may change, but it is not resolvable by our HRTEM due to the very small diameter of Li ions and therefore does not affect the DIC analysis.

Across the lithiation front, the reaction of Li with Si causes a change in the Li:Si molar ratio from zero to a finite value. The deformation induced by the reaction exhibits a large strain gradient at the sharp reaction front, which is unresolvable by the local DIC method. The use of local DIC in this case would result in underestimation of the deformation gradient. To obtain the reaction-induced strain, we adopted the global DIC approach using an analytical trial deformation field as follows:

$$\varepsilon_{xx} = \varepsilon_{xy} = 0 \tag{7a}$$

$$\varepsilon_{yy}(y) = \frac{\varepsilon_R}{2}\left[\operatorname{erf}\left(\frac{y - y_1}{a}\right) - \operatorname{erf}\left(\frac{y - y_2}{a}\right)\right] \tag{7b}$$

where ε_R is the reaction-induced strain, y_1 and y_2 are the starting and ending positions of the reaction zone defined in the reference

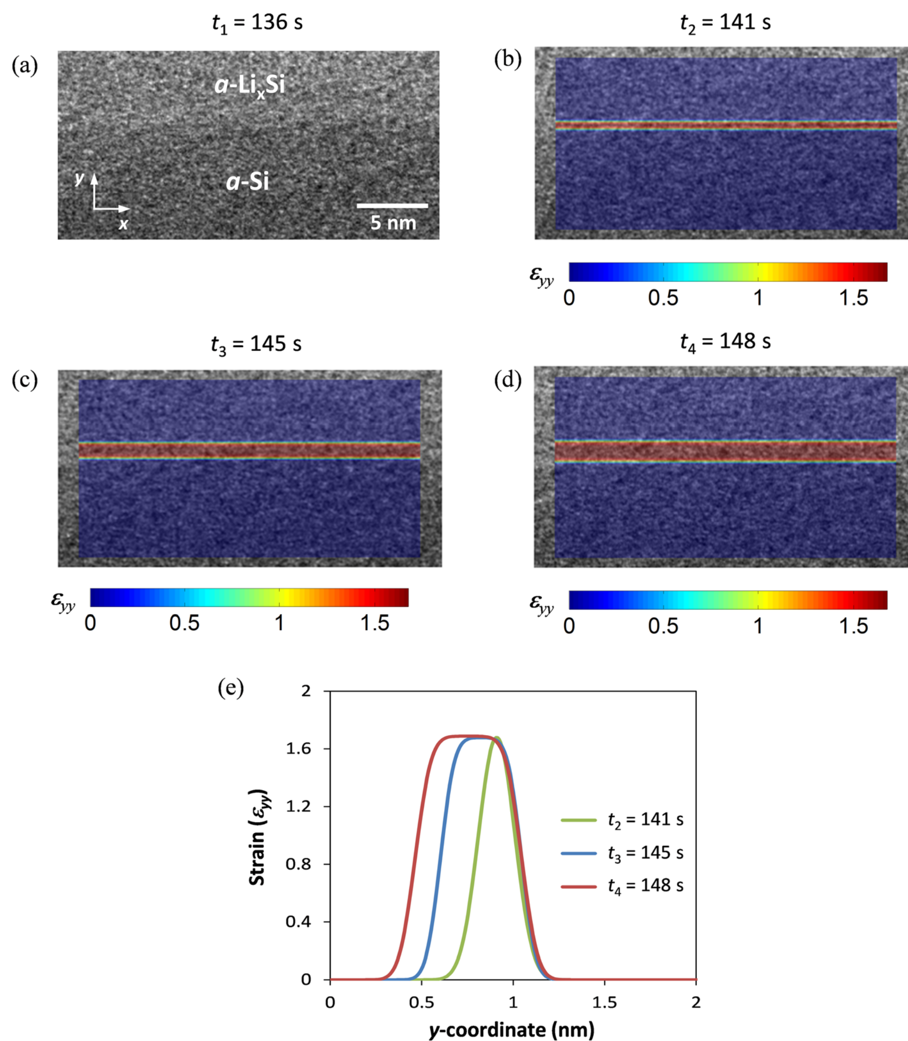

Fig. 7 Global DIC analysis of the reaction-induced strain at an *a*-Si/*a*-Li_xSi phase boundary. (*a*) The first image in a sequence of TEM images serving as the reference image for the global DIC analysis. ((*b*)–(*d*)) Obtained ε_{yy} strain contour plots superimposed on the subsequent TEM images at various stages of lithiation. (*e*) Obtained strain profiles across the *a*-Si/*a*-Li_xSi phase boundary. Note that the strain analysis is made with respect to the reference image in (*a*). The width of the reaction zone with large strain increases as the lithiation proceeds.

Downloaded From: http://appliedmechanics.asmedigitalcollection.asme.org/ on 09/10/2015 Terms of Use: http://www.asme.org/about-asme/terms-of-use

configuration, a is the half-width of the strain gradient zone, and the $\mathrm{erf}(\cdot)$ function is the Gauss error function. In choosing the above trial deformation field, we have two considerations that arise from the local DIC result. First, there is no appreciable deformation in the x-direction due to the lateral constraint of the unreacted a-Si region, such that the DIC problem can be treated as one-dimensional. Second, the diffusion-induced strain in the a-Li_xSi region is negligibly small, leading to a nearly rigid-body movement of the a-Li_xSi region. By integrating Eq. (7), the trial displacement field is obtained as

$$u_x = u_x^0 \tag{8a}$$

$$u_y(y) = \frac{\varepsilon_R}{2}\left\{(y-y_1)\mathrm{erf}\left(\frac{y-y_1}{a}\right) - (y-y_2)\mathrm{erf}\left(\frac{y-y_2}{a}\right) + \frac{a}{\sqrt{\pi}}\left[e^{-\frac{(y-y_1)^2}{a^2}} - e^{-\frac{(y-y_2)^2}{a^2}}\right] + (y_2-y_1)\right\} + u_y^0 \tag{8b}$$

in which u_x^0 and u_y^0 are the rigid-body displacement components of the unreacted a-Si region. Figures 6(a) and 6(b) show schematically the trial displacement and strain profiles as a function of the y-coordinate.

A global DIC analysis was performed on the same reference (Fig. 7(a)) and deformed (Fig. 7(d)) images used for the previous local DIC analysis. Additionally, we sought to obtain an evolution of the reaction-induced strain by correlating two intermediate frames (Figs. 7(b) and 7(c)) at time instants $t_2 = 141$ s and $t_3 = 145$ s to the reference frame. At each time instant, the error functional defined in Eq. (4) was minimized with respect to the parameter set (ε_R, y_1, y_2, a, u_x^0, and u_y^0) of the trial displacement function. The minimization was carried out over a rectangular region of 12×24 nm around the a-Si/a-Li_xSi boundary using a simplex search method of Lagarias et al. [65]. The distributions of reaction-induced strain resulting from the minimization process are presented in Figs. 7(b)–7(d), and Fig. 7(e) shows the strain profiles across the a-Si/a-Li_xSi phase boundary. The lithiation front is seen to move steadily toward the a-Si region at a speed of 0.05 nm/s. Inside the reaction zone, the reaction-induced strain reaches a maximum value of $\varepsilon_R = 168\%$, which remains fairly constant as the lithiation proceeds. Invoking a linear relationship between the volumetric strain and lithium concentration [66–68], $\varepsilon = 0.72x$, we obtain a molar Li:Si ratio of $x = 2.33$ in the reaction zone. Also note from Fig. 7(e) that the width of the strain gradient zones (i.e., the zones over which the strain increases from 0% to 168%) is 0.32 nm, which is comparable to the average Si–Si bond length of 0.23–0.25 nm in a-Si [69–71]; this suggests that the a-Si/a-Li_xSi phase boundary is atomistically sharp. Finally, we note that the lithiation process in a-Si revealed by the in situ TEM experiments [50] is a two-step process. In this work, we focused on the first lithiation step in which a-Si is transformed into a-$Li_{2.33}$Si through a two-phase lithiation mechanism. In the second step of lithiation, the phase of a-$Li_{2.33}$Si is further transformed into the fully lithiated phase of a-$Li_{3.75}$Si. This step of lithiation proceeded very fast, such that we could not acquire high-quality TEM images for DIC analysis. Future investigation with a better control of the second-step lithiation is required to elucidate the lithiation mechanism in this step [50].

5 Conclusions

We have shown that it is feasible to combine high-resolution TEM and DIC for performing full-field deformation analysis at the nanoscale. The theories behind two different DIC methods—local and global DIC—were introduced, and their advantages and disadvantages were discussed. A quantitative error assessment was made by correlating TEM images captured during the rigid-body movement of an a-Si specimen. It was shown that the strain errors resulting from the TEM image noise and electromagnetic-lens distortion were on the order of 0.1%. The utility of TEM-DIC was demonstrated through a case study of two-phase lithiation in a-Si. The local and global DIC were applied to analyze the diffusion-induced strain in the lithiated Si region and the reaction-induced strain at the lithiation front, respectively. The DIC analysis revealed that the lithiation in a-Si occurred by the movement of an atomistically sharp phase boundary between the a-Si reactant and an amorphous a-Li_xSi ($x = 2.33$) product. Broadly, the TEM-DIC technique presented in this work enables the analysis of full-field deformation at considerably smaller length scales than other microscope-based DIC methods, and thus provides a new avenue for nanoscale material characterization.

Acknowledgment

S.X. acknowledges the support from the NSF Grant No. CMMI-1300458. T.Z. acknowledges the support from the NSF Grant Nos. CMMI-1100205 and DMR-1410936. S.X.M. acknowledges the support from the NSF Grant No. CMMI-08010934 through the University of Pittsburgh and Sandia National Lab. This work was performed, in part, at the Center for Integrated Nanotechnologies, a U.S. Department of Energy, Office of Basic Energy Sciences user facility. Sandia National Laboratories is a multiprogram laboratory managed and operated by Sandia Corporation, a wholly owned subsidiary of Lockheed Martin Corporation, for the U.S. Department of Energy's National Nuclear Security Administration under Contract No. DE-AC04-94AL85000.

References

[1] Johnson, C., Ruud, J., Bruce, R., and Wortman, D., 1998, "Relationships Between Residual Stress, Microstructure and Mechanical Properties of Electron Beam–Physical Vapor Deposition Thermal Barrier Coatings," Surf. Coat. Technol., **108–109**, pp. 80–85.

[2] Nave, M. D., and Barnett, M. R., 2004, "Microstructures and Textures of Pure Magnesium Deformed in Plane-Strain Compression," Scr. Mater., **51**(9), pp. 881–885.

[3] Rastogi, P., 2000, *Photomechanics*, Springer, Berlin.

[4] Grediac, M., 2004, "The Use of Full-Field Measurement Methods in Composite Material Characterization: Interest and Limitations," Composites, Part A, **35**(7), pp. 751–761.

[5] Hung, Y., and Ho, H., 2005, "Shearography: An Optical Measurement Technique and Applications," Mater. Sci. Eng.: R, **49**(3), pp. 61–87.

[6] Avril, S., Bonnet, M., Bretelle, A.-S., Grediac, M., Hild, F., Ienny, P., Latourte, F., Lemosse, D., Pagano, S., and Pagnacco, E., 2008, "Overview of Identification Methods of Mechanical Parameters Based on Full-Field Measurements," Exp. Mech., **48**(4), pp. 381–402.

[7] McClung, A. J., Tandon, G., Goecke, K., and Baur, J., 2011, "Non-Contact Technique for Characterizing Full-Field Surface Deformation of Shape Memory Polymers at Elevated and Room Temperatures," Polym. Test., **30**(1), pp. 140–149.

[8] Chu, T., Ranson, W., and Sutton, M., 1985, "Applications of Digital-Image-Correlation Techniques to Experimental Mechanics," Exp. Mech., **25**(3), pp. 232–244.

[9] Pan, B., Qian, K., Xie, H., and Asundi, A., 2009, "Two-Dimensional Digital Image Correlation for In-Plane Displacement and Strain Measurement: A Review," Meas. Sci. Technol., **20**(6), p. 062001.

[10] Peters, W. H., and Ranson, W. F., 1982, "Digital Imaging Techniques in Experimental Stress-Analysis," Opt. Eng., **21**(3), pp. 427–431.

[11] Sutton, M. A., Cheng, M. Q., Peters, W. H., Chao, Y. J., and Mcneill, S. R., 1986, "Application of an Optimized Digital Correlation Method to Planar Deformation Analysis," Image Vision Comput., **4**(3), pp. 143–150.

[12] Delacourt, C., Allemand, P., Casson, B., and Vadon, H., 2004, "Velocity Field of the 'La Clapière' Landslide Measured by the Correlation of Aerial and QuickBird Satellite Images," Geophys. Res. Lett., **31**(15), p. L15619.

[13] Krehbiel, J. D., Lambros, J., Viator, J., and Sottos, N., 2010, "Digital Image Correlation for Improved Detection of Basal Cell Carcinoma," Exp. Mech., **50**(6), pp. 813–824.

[14] Chasiotis, I., and Knauss, W. G., 2002, "A New Microtensile Tester for the Study of MEMS Materials With the Aid of Atomic Force Microscopy," Exp. Mech., **42**(1), pp. 51–57.

[15] Knauss, W. G., Chasiotis, I., and Huang, Y., 2003, "Mechanical Measurements at the Micron and Nanometer Scales," Mech. Mater., **35**(3–6), pp. 217–231.

[16] Chasiotis, I., 2004, "Mechanics of Thin Films and Microdevices," IEEE Trans. Device Mater. Reliab., **4**(2), pp. 176–188.

[17] Cho, S., Chasiotis, I., Friedmann, T. A., and Sullivan, J. P., 2005, "Young's Modulus, Poisson's Ratio and Failure Properties of Tetrahedral Amorphous Diamond-Like Carbon for MEMS Devices," J. Micromech. Microeng., **15**(4), pp. 728–735.

Downloaded From: http://appliedmechanics.asmedigitalcollection.asme.org/ on 09/10/2015 Terms of Use: http://www.asme.org/about-asme/terms-of-use

[18] Cho, S., Cárdenas-García, J. F., and Chasiotis, I., 2005, "Measurement of Nano-displacements and Elastic Properties of MEMS Via the Microscopic Hole Method," Sens. Actuators, A, **120**(1), pp. 163–171.
[19] Chang, S., Wang, C. S., Xiong, C. Y., and Fang, J., 2005, "Nanoscale In-Plane Displacement Evaluation by AFM Scanning and Digital Image Correlation Processing," Nanotechnology, **16**(4), pp. 344–349.
[20] Sun, Y., and Pang, J. H., 2006, "AFM Image Reconstruction for Deformation Measurements by Digital Image Correlation," Nanotechnology, **17**(4), pp. 933–939.
[21] Cho, S. W., and Chasiotis, I., 2007, "Elastic Properties and Representative Volume Element of Polycrystalline Silicon for MEMS," Exp. Mech., **47**(1), pp. 37–49.
[22] Li, X. D., Xu, W. J., Sutton, M. A., and Mello, M., 2007, "In Situ Nanoscale In-Plane Deformation Studies of Ultrathin Polymeric Films During Tensile Deformation Using Atomic Force Microscopy and Digital Image Correlation Techniques," IEEE Trans. Nanotechnol., **6**(1), pp. 4–12.
[23] Sun, Y., Pang, J. H., and Fan, W., 2007, "Nanoscale Deformation Measurement of Microscale Interconnection Assemblies by a Digital Image Correlation Technique," Nanotechnology, **18**(39), p. 395504.
[24] Vendroux, G., and Knauss, W., 1998, "Submicron Deformation Field Measurements: Part 1. Developing a Digital Scanning Tunneling Microscope," Exp. Mech., **38**(1), pp. 18–23.
[25] Vendroux, G., and Knauss, W., 1998, "Submicron Deformation Field Measurements: Part 2. Improved Digital Image Correlation," Exp. Mech., **38**(2), pp. 86–92.
[26] Vendnroux, G., Schmidt, N., and Knauss, W., 1998, "Submicron Deformation Field Measurements: Part 3. Demonstration of Deformation Determinations," Exp. Mech., **38**(3), pp. 154–160.
[27] Kang, J., Jain, M., Wilkinson, D. S., and Embury, J. D., 2005, "Microscopic Strain Mapping Using Scanning Electron Microscopy Topography Image Correlation at Large Strain," J. Strain Anal. Eng. Des., **40**(6), pp. 559–570.
[28] Sabate, N., Vogel, D., Gollhardt, A., Keller, J., Michel, B., Cane, C., Gracia, I., and Morante, J. R., 2006, "Measurement of Residual Stresses in Micromachined Structures in a Microregion," Appl. Phys. Lett., **88**(7), p. 071910.
[29] Lagattu, F., Bridier, F., Villechaise, P., and Brillaud, J., 2006, "In-Plane Strain Measurements on a Microscopic Scale by Coupling Digital Image Correlation and an In Situ SEM Technique," Mater. Charact., **56**(1), pp. 10–18.
[30] Sutton, M. A., Li, N., Garcia, D., Cornille, N., Orteu, J. J., McNeill, S. R., Schreier, H. W., and Li, X., 2006, "Metrology in a Scanning Electron Microscope: Theoretical Developments and Experimental Validation," Meas. Sci. Technol., **17**(10), pp. 2613–2622.
[31] Sutton, M., Li, N., Joy, D., Reynolds, A., and Li, X., 2007, "Scanning Electron Microscopy for Quantitative Small and Large Deformation Measurements Part I: SEM Imaging at Magnifications From 200 to 10,000," Exp. Mech., **47**(6), pp. 775–787.
[32] Sutton, M. A., Li, N., Garcia, D., Cornille, N., Orteu, J., McNeill, S., Schreier, H., Li, X., and Reynolds, A. P., 2007, "Scanning Electron Microscopy for Quantitative Small and Large Deformation Measurements Part II: Experimental Validation for Magnifications From 200 to 10,000," Exp. Mech., **47**(6), pp. 789–804.
[33] Kammers, A. D., and Daly, S., 2013, "Digital Image Correlation Under Scanning Electron Microscopy: Methodology and Validation," Exp. Mech., **53**(9), pp. 1743–1761.
[34] Kammers, A. D., and Daly, S., 2013, "Self-Assembled Nanoparticle Surface Patterning for Improved Digital Image Correlation in a Scanning Electron Microscope," Exp. Mech., **53**(8), pp. 1333–1341.
[35] Guo, S., Sutton, M., Li, X., Li, N., and Wang, L., 2014, "SEM-DIC Based Nanoscale Thermal Deformation Studies of Heterogeneous Material," *Advancement of Optical Methods in Experimental Mechanics*, Vol. 3, Springer, New York, pp. 145–150.
[36] Jin, H., Lu, W., and Korellis, J., 2008, "Micro-Scale Deformation Measurement Using the Digital Image Correlation Technique and Scanning Electron Microscope Imaging," J. Strain Anal. Eng. Des., **43**(8), pp. 719–728.
[37] Tschopp, M., Bartha, B., Porter, W., Murray, P., and Fairchild, S., 2009, "Microstructure-Dependent Local Strain Behavior in Polycrystals Through In-Situ Scanning Electron Microscope Tensile Experiments," Metall. Mater. Trans. A, **40**(10), pp. 2363–2368.
[38] Sabate, N., Vogel, D., Gollhardt, A., Keller, J., Cane, C., Gracia, I., Morante, J. R., and Michel, B., 2007, "Residual Stress Measurement on a MEMS Structure With High-Spatial Resolution," J. Microelectromech. Syst., **16**(2), pp. 365–372.
[39] Wang, Z., 2000, "Transmission Electron Microscopy of Shape-Controlled Nanocrystals and Their Assemblies," J. Phys. Chem. B, **104**(6), pp. 1153–1175.
[40] Williams, D. B., and Carter, C. B., 2009, *Transmission Electron Microscopy*, Springer, New York.
[41] Hÿtch, M., Snoeck, E., and Kilaas, R., 1998, "Quantitative Measurement of Displacement and Strain Fields From HREM Micrographs," Ultramicroscopy, **74**(3), pp. 131–146.
[42] Snoeck, E., Warot, B., Ardhuin, H., Rocher, A., Casanove, M., Kilaas, R., and Hÿtch, M., 1998, "Quantitative Analysis of Strain Field in Thin Films From HRTEM Micrographs," Thin Solid Films, **319**(1), pp. 157–162.
[43] Hÿtch, M., Houdellier, F., Hüe, F., and Snoeck, E., 2008, "Nanoscale Holographic Interferometry for Strain Measurements in Electronic Devices," Nature, **453**(7198), pp. 1086–1089.
[44] Zhang, P., Istratov, A. A., Weber, E. R., Kisielowski, C., He, H., Nelson, C., and Spence, J. C., 2006, "Direct Strain Measurement in a 65 nm Node Strained Silicon Transistor by Convergent-Beam Electron Diffraction," Appl. Phys. Lett., **89**(16), p. 161907.
[45] Jones, P., Rackham, G., and Steeds, J., 1977, "Higher Order Laue Zone Effects in Electron Diffraction and Their Use in Lattice Parameter Determination," Proc. R. Soc. London, Ser. A, **354**(1677), pp. 197–222.
[46] Armigliato, A., Balboni, R., Carnevale, G., Pavia, G., Piccolo, D., Frabboni, S., Benedetti, A., and Cullis, A., 2003, "Application of Convergent Beam Electron Diffraction to Two-Dimensional Strain Mapping in Silicon Devices," Appl. Phys. Lett., **82**(13), pp. 2172–2174.
[47] Usuda, K., Numata, T., Irisawa, T., Hirashita, N., and Takagi, S., 2005, "Strain Characterization in SOI and Strained-Si on SGOI MOSFET Channel Using Nano-Beam Electron Diffraction (NBD)," Mater. Sci. Eng.: B, **124–125**, pp. 143–147.
[48] Uesugi, F., Hokazono, A., and Takeno, S., 2011, "Evaluation of Two-Dimensional Strain Distribution by STEM/NBD," Ultramicroscopy, **111**(8), pp. 995–998.
[49] Orlov, A., Granovsky, A., Balagurov, L., Kulemanov, I., Parkhomenko, Y. N., Perov, N., Gan'shina, E., Bublik, V., Shcherbachev, K., and Kartavykh, A., 2009, "Structure, Electrical and Magnetic Properties, and the Origin of the Room Temperature Ferromagnetism in Mn-Implanted Si," J. Exp. Theor. Phys., **109**(4), pp. 602–608.
[50] Wang, J. W., He, Y., Fan, F., Liu, X. H., Xia, S., Liu, Y., Harris, C. T., Li, H., Huang, J. Y., Mao, S. X., and Zhu, T., 2013, "Two-Phase Electrochemical Lithiation in Amorphous Silicon," Nano Lett., **13**(2), pp. 709–715.
[51] Peters, W., and Ranson, W., 1982, "Digital Imaging Techniques in Experimental Stress Analysis," Opt. Eng., **21**(3), pp. 427–431.
[52] Sutton, M., Wolters, W., Peters, W., Ranson, W., and McNeill, S., 1983, "Determination of Displacements Using an Improved Digital Correlation Method," Image Vision Comput., **1**(3), pp. 133–139.
[53] Lu, H., and Cary, P., 2000, "Deformation Measurements by Digital Image Correlation: Implementation of a Second-Order Displacement Gradient," Exp. Mech., **40**(4), pp. 393–400.
[54] Bornert, M., Brémand, F., Doumalin, P., Dupré, J.-C., Fazzini, M., Grédiac, M., Hild, F., Mistou, S., Molimard, J., and Orteu, J.-J., 2009, "Assessment of Digital Image Correlation Measurement Errors: Methodology and Results," Exp. Mech., **49**(3), pp. 353–370.
[55] Bruck, H., McNeill, S., Sutton, M. A., and Peters Iii, W., 1989, "Digital Image Correlation Using Newton–Raphson Method of Partial Differential Correction," Exp. Mech., **29**(3), pp. 261–267.
[56] Sun, Y., Pang, J. H., Wong, C. K., and Su, F., 2005, "Finite Element Formulation for a Digital Image Correlation Method," Appl. Opt., **44**(34), pp. 7357–7363.
[57] Besnard, G., Hild, F., and Roux, S., 2006, "'Finite-Element' Displacement Fields Analysis From Digital Images: Application to Portevin–Le Châtelier Bands," Exp. Mech., **46**(6), pp. 789–803.
[58] Réthoré, J., Roux, S., and Hild, F., 2010, "Hybrid Analytical and Extended Finite Element Method (HAX-FEM): A New Enrichment Procedure for Cracked Solids," Int. J. Numer. Methods Eng., **81**(3), pp. 269–285.
[59] Réthoré, J., Roux, S., and Hild, F., 2010, "Mixed-Mode Crack Propagation Using a Hybrid Analytical and Extended Finite Element Method," C. R. Méc., **338**(3), pp. 121–126.
[60] Williams, M. L., 1957, "On the Stress Distribution at the Base of a Stationary Crack," ASME J. Appl. Mech., **24**(1), pp. 109–114.
[61] Hild, F., and Roux, S., 2012, "Comparison of Local and Global Approaches to Digital Image Correlation," Exp. Mech., **52**(9), pp. 1503–1519.
[62] Pan, B., Wang, B., Lubineau, G., and Moussawi, A., 2015, "Comparison of Subset-Based Local and Finite Element-Based Global Digital Image Correlation," Exp. Mech., **55**(5), pp. 887–901.
[63] Reimer, L., 2013, *Transmission Electron Microscopy: Physics of Image Formation and Microanalysis*, Springer, New York.
[64] Muller, D. A., Kirkland, E. J., Thomas, M. G., Grazul, J. L., Fitting, L., and Weyland, M., 2006, "Room Design for High-Performance Electron Microscopy," Ultramicroscopy, **106**(11), pp. 1033–1040.
[65] Lagarias, J. C., Reeds, J. A., Wright, M. H., and Wright, P. E., 1998, "Convergence Properties of the Nelder–Mead Simplex Method in Low Dimensions," SIAM J. Optim., **9**(1), pp. 112–147.
[66] Beaulieu, L., Hatchard, T., Bonakdarpour, A., Fleischauer, M., and Dahn, J., 2003, "Reaction of Li With Alloy Thin Films Studied by In Situ AFM," J. Electrochem. Soc., **150**(11), pp. A1457–A1464.
[67] He, Y., Yu, X., Li, G., Wang, R., Li, H., Wang, Y., Gao, H., and Huang, X., 2012, "Shape Evolution of Patterned Amorphous and Polycrystalline Silicon Microarray Thin Film Electrodes Caused by Lithium Insertion and Extraction," J. Power Sources, **216**, pp. 131–138.
[68] Becker, C. R., Strawhecker, K. E., McAllister, Q. P., and Lundgren, C. A., 2013, "In Situ Atomic Force Microscopy of Lithiation and Delithiation of Silicon Nanostructures for Lithium Ion Batteries," ACS Nano, **7**(10), pp. 9173–9182.
[69] Laaziri, K., Kycia, S., Roorda, S., Chicoine, M., Robertson, J., Wang, J., and Moss, S., 1999, "High-Energy X-Ray Diffraction Study of Pure Amorphous Silicon," Phys. Rev. B, **60**(19), pp. 13520–13533.
[70] Wakagi, M., Ogata, K., and Nakano, A., 1994, "Structural Study of a-Si and a-Si: H Films by EXAFS and Raman-Scattering Spectroscopy," Phys. Rev. B, **50**(15), pp. 10666–10671.
[71] Kugler, S., Pusztai, L., Rosta, L., Chieux, P., and Bellissent, R., 1993, "Structure of Evaporated Pure Amorphous Silicon: Neutron-Diffraction and Reverse Monte Carlo Investigations," Phys. Rev. B, **48**(10), pp. 7685–7688.

Downloaded From: http://appliedmechanics.asmedigitalcollection.asme.org/ on 09/10/2015 Terms of Use: http://www.asme.org/about-asme/terms-of-use